PAPER • **OPEN ACCESS**

Enabling electrical response through piezoelectric particle integration in AA2017-T451 aluminium parts using FSP technology

To cite this article: Pedro M Ferreira *et al* 2024 *Smart Mater. Struct.* **33** 065037

OPEN ACCESS
IOP Publishing
Smart Materials and Structures
Smart Mater. Struct. **33** (2024) 065037 (20pp)
https://doi.org/10.1088/1361-665X/ad4d45

Enabling electrical response through piezoelectric particle integration in AA2017-T451 aluminium parts using FSP technology

Pedro M Ferreira[1,*], David Caçador[1], Miguel A Machado[1,2], Marta S Carvalho[1,2], Pedro Vilaça[3], Gonçalo Sorger[3], Francisco Werley Cipriano Farias[1], Arthur Ribeiro Figueiredo[4] and Catarina Vidal[1,2]

[1] UNIDEMI, Department of Mechanical and Industrial Engineering, NOVA School of Science and Technology, Universidade NOVA de Lisboa, 2829-516 Caparica, Portugal
[2] Laboratório Associado de Sistemas Inteligentes, LASI, 4800-058 Guimarães, Portugal
[3] Department of Mechanical Engineering, School of Engineering, Aalto University, PO Box 14200, FI-00076 Espoo, Finland
[4] Program of Metallurgical and Materials Engineering, Federal University of Rio de Janeiro (UFRJ), CEP 21941-972 Rio de Janeiro, RJ, Brazil

E-mail: pdm.ferreira@campus.fct.unl.pt

Received 8 March 2024, revised 7 May 2024
Accepted for publication 17 May 2024
Published 29 May 2024

Abstract

In the field of structural engineering, the integration of smart materials and structural health monitoring (SHM) has given rise to self-sensing materials (SSM), leading to a paradigm shift in SHM. This paper focuses on the interplay between self-sensing capabilities and the piezoelectric properties of lead zirconate titanate (PZT) and barium titanate (BT) in aluminium components. Leveraging Friction Stir Processing (FSP), the study explores the synthesis and performance of SSMs with embedded piezoelectric particles, potentially transforming structural engineering. The paper highlights FSP as a key methodology for incorporating piezoelectric particles into structural materials, showcasing its potential in developing SSMs with enhanced functionalities. A specific focus is placed on integrating PZT and BT particles into AA2017-T451 aluminium parts using FSP, with metallographic assessments and mechanical property evaluations conducted to analyse particle distribution and concentration. This study shows how BT and PZT particles are incorporated into AA2017-T451 aluminium to create a SSM that responds to external stimuli. Under cyclic loading, the SSMs exhibit a linear load-electrical response correlation, with sensibility increasing at lower frequencies. Metallographic analysis shows homogeneous particle distribution, while PZT induces increased brittleness and brittle fractures. Yield strength remains relatively stable, but ultimate strength decreases post-FSP. Hardness variations indicate weaker bonding with PZT particles. Eddy's

* Author to whom any correspondence should be addressed.

current testing aligns with hardness profiles, and sensorial characterization reveals a non-linear frequency-sensibility relationship, showcasing the SSMs' suitability for low-frequency applications, particularly with PZT embedment.

Keywords: self-sensing material, piezoelectric materials, friction stir processing, advanced materials, structural health monitoring

1. Introduction

In the field of structural engineering the perpetual pursuit of innovative materials and methodologies that enhance the durability, adaptability, and longevity of infrastructural systems has led to a transformative paradigm in recent years [1, 2]. The convergence of smart materials and structural health monitoring (SHM) has empowered structures to actively sense, assess, and respond to changes in operational conditions [3–8]. A focal point of this advancement is the rise of self-sensing materials (SSM), which can autonomously detect changes in structural conditions and materials behaviour.

The piezoelectric effect, discovered by the Curie brothers in 1880, was first applied to ultrasound technology during World War I using quartz crystal transducers. Later, the development of piezoelectric ceramics like lead zirconate titanate (PZT) and barium titanate (BT) revolutionized the sensing technology. These piezoelectric ceramics allowed to obtain more flexible shapes and sizes, produced through sintering, with enhanced properties when polarized. Today, PZT and BT are the leading piezoelectric ceramics used in various applications, such as, energy harvesting and ultrasonic transducers [9–11]. Consequently, this study will utilize PZT and BT particles, as they are widely used. Other piezoelectric materials, such as Lead Titanate and Lead Magnesium Niobate, serve specific needs like high-temperature transducers. Beyond ceramics, piezoelectric materials include quartz crystals, composites, monocrystals, semiconductors, and polymers, providing a diverse range of applications in industry and technology [2, 12, 13]. Piezoelectric materials like PZT and BT are valued for their ability to convert mechanical stress into electrical energy and vice versa. They are widely used across civil, mechanical, and aerospace engineering. In civil engineering, they monitor structural health [14, 15]; in mechanical engineering, they provide precision actuation [16]; and in aerospace, they help with vibration control and energy harvesting [17, 18]. These materials offer enhanced safety, efficiency, and performance across industries.

This paper delves into the intricate interplay between self-sensing capabilities and the piezoelectric properties of PZT and BT, with a particular focus on their potential application in aluminium components. Aluminium, widely used for its lightweight and corrosion-resistant properties in aerospace, automotive, and structural applications, holds significant promise for implementing advanced SHM technologies [19–22].

Recent progress in piezoelectric materials and manufacturing methods at the micro and nanoscale have broadened the application fields of piezoelectric technology. Materials like ceramics [23, 24], polymers [25, 26], composites [27, 28], and biocompatible materials [5, 29], in diverse nanostructures [30, 31] and thin films [32, 33], exhibit satisfactory physical properties such as high piezoelectric coefficients, flexibility, stretchability, and durability. This study explores the principles of piezoelectricity and the choice of materials, emphasizing the role of piezoceramics and piezoelectric composites in SHM.

A key methodology in the synthesis of these advanced materials is friction stir processing (FSP) [34–42], a novel approach for incorporating piezoelectric particles into structural materials. This investigation explores the mechanics and advantages of employing FSP, showcasing its potential to develop SSMs with enhanced functionalities. The synergy between FSP, metallic parts, and piezoelectric particles underscores the interdisciplinary nature of materials science, structural engineering, and advanced manufacturing.

Recent studies [43–45] highlighted the influence of introducing piezoelectric ceramic particles into a metallic component, impacting both its mechanical properties and inducing an electrical response under various conditions. These studies specifically focus on integrating piezoelectric particles into aluminium parts (AA2017-T451) using FSP technology, utilizing BT and PZT particles to enhance the sensitivity and technical aspects of the resulting SSM. Different FSP variants, such as those presented by Vidal *et al* [46] and Moreira *et al* [47], allow particle incorporation in the metallic matrix. Metallographic assessments and mechanical property evaluations were conducted to analyse particle distribution, concentration, and their impact on the base material's mechanical behaviour. Additionally, the study comprehensively examined the SSM's sensorial properties and sensitivity.

This research aims to deepen our understanding of SSM applications and optimize their properties, paving the way for advanced materials in various industries. The transformative process involves strategically incorporating piezoelectric particles into metallic components through the innovative FSP technique, endowing aluminium components with the unique capability to exhibit an electrical response to cyclic mechanical loads. This inherent electrical response serves as a sophisticated monitoring mechanism, offering real-time insights into the component's stress and strain throughout

its entire lifecycle. Future efforts must effectively implement and deploy this technology for the comprehensive lifecycle monitoring of metallic components. The integration of piezoelectric particles, leveraging their ability to generate electric charge in response to loads, expands the materials available for SHM. This ability is also capitalized due to the inherent properties of piezoelectric particles, which are known for their high piezoelectric coefficients and applicability for a wide range of applications [48, 49]. This paper aims to uncover the underlying principles governing the synthesis and performance of SSMs with embedded piezoelectric particles in aluminium parts, shedding light on their potential transformative impact on structural engineering.

2. Materials and methods

2.1. Materials

To impart sensorial attributes to the AA2017-T451 plates the incorporation of PZT and BT particles was conducted through FSP, following the outlined procedure in [45]. The base plate underwent the T451 heat treatment in its as-revised condition. This involved subjecting the plate to a solution heat treatment, followed by a stress-relieving step achieved through controlled stretching (1.5% and 3% for plates). Finally, the plate underwent natural ageing following the T451 tempers [3, 50, 51]. The chemical compositions of the AA2017-T451 plates are delineated in table 1. Copper (Cu) emerges as the principal alloying element in AA2017-T451, a conventionally integrated component in 2xxx aluminium alloys to augment mechanical strength through precipitation hardening. The dimensions of the AA2017-T451 aluminium plates utilized for SSMs fabrication are 203 mm (rolling direction) $\times$ 103 mm $\times$ 8 mm. The mechanical and physical properties of the aluminium plates are presented in table 2.

As previously elucidated, to confer sensorial attributes to the aluminium substrate, BT and PZT piezoelectric particles were integrated. The BT particles ($BaTiO_3$), boasting a purity of 99.7%, exhibit a homogeneous granular morphology with a particle size smaller than 2 μm [43–45]. The PZT particles, with a purity of 99.9% and varying in size from sub-micron dimensions to approximately 20 μm, tend to form agglomerates, as opposed to the more discrete nature of the BT particles [43–45]. These particles (BT and PZT) are commercially available and were manufactured by Alfa Aesar and Nanoshel Ltd, respectively.

Both BT and PZT particles are piezoelectric ceramics encompassing numerous microscopic ferroelectric crystals. These crystals exhibit a perovskite crystalline structure, with the ability to assume tetragonal, rhombohedral, orthorhombic, or simple cubic phases contingent upon the temperature to which they are exposed, denoted as the Curie temperature. The piezoelectric and physical properties of BT and PZT piezoelectric particles are detailed in table 3. The piezoelectric constants (d_{33}, d_{31}) and the electromechanical coupling coefficients (k_{33}, k_{31}) are noteworthy properties, with the former and the latter being manifested when stress is parallel and perpendicular to the dipole moment, respectively, resulting in altered spontaneous polarization and transverse electrical charge.

2.2. Methods

The incorporation of PZT and BT particles into the aluminium matrix through FSP was carried out following the procedure outlined in [45] (figure 1(a)). The groove dimensions, as illustrated in figure 1(a), were chosen based on their most favourable response to cyclic loading, as previously reported in [45]. A series of FSP tools were utilized in the material processing. The first tool used was a pinless FSP tool with a left-hand scrolled shoulder, and the second tool was a pinned FSP tool with a featureless concave shoulder and a triflute left-handed conical pin. In sequence, to compact the particles into the groove, a pass with the pinless FSP tool was executed to seal the groove and contain the particles. This was followed by four consecutive passes with the pinned FSP tool, all in the same direction. Subsequently, a polarization process was conducted in a controlled environment at 90 °C, applying a strong electrical field (9 kV) to induce orientation in the previously disorganized electrical dipole arrangements. Figure 1(a) illustrates the FSP process for incorporating the piezoelectric particles.

The selection of FSP parameters was informed by a small study to ensure optimal particle distribution. Additionally, a supplementary plate (AA2017-R) was manufactured without any particles for comparative analysis with the results of SSM based on PZT (AA2017-PZT) and BT (AA2017-BT) particles.

Temperature measurements during the SSM manufacturing process were performed using six K-type thermocouples positioned between the backing plate and the AA2017-T451 plate. Three thermocouples were placed on the advancing side (AS), and the remaining three were on the retreating side (RS), as depicted in figure 1(b). Surface temperature measurements were conducted using a Fluke Ti400 infrared camera. The temperature measurements were carried out to provide an in-depth comprehension of the impact of FSP on the production of SSMs.

Post-SSM processing, samples were prepared for various characterization techniques (figure 1(c)). Macro and micrography, as well as x-ray microtomography (μCT) samples, were polished following standard metallographic procedures. Macro and micrography samples were etched in Keller reagent (2 ml HF, 3 ml HCl, 20 ml HNO_3, and 175 ml H_2O). Optical analyses of macro and microstructures were performed using a Leica DMI 5000 M inverted optical microscope to examine the distribution of particles. The 3D and 2D micro-architectural morphology of the SSM, based on PZT and BT particles,

Table 1. AA2017-T451 plates' chemical composition (wt%) (from datasheet).

Elements	Si	Fe	Cu	Mn	Mg	Cr	Zn	Ti + Zr	Al
Min	0.2	—	3.5	0.4	0.4	—	—	—	—
Max	0.8	0.7	4.5	1	1	0.1	0.25	0.25	Remaining

Table 2. Mechanical and physical properties of AA2017-T451 (from datasheet).

Properties	AA2017-T451
Yield strength, $\sigma_{0.2}$ (MPa)	260
Modulus of elasticity, E (GPa)	72
Ultimate tensile strength, σ_{UTS} (MPa)	390
Vickers hardness (HV)	118

Table 3. Piezoelectric and physical properties of $BaTiO_3$ and $PbTiZrO_5$ [43–45].

Properties	$BaTiO_3$	$PbTiZrO_5$
Dielectric constant (K_{33})	1700	1300
Piezoelectric constant (d_{33}, d_{31}) (pC N^{-1})	190, −78	270, −120
Electromechanical coupling coefficient (k_{33}, k_{31})	0.50, 0.21	0.71, −0.34
Curie temperature (T_c) (C)	115	300–370

was characterized using μCT with a Phoenix V|TOME|X, GE, according to the procedure conducted by Vidal *et al* [52]. The acquired image data were qualitatively and quantitatively interpreted using 3D tomographic reconstruction and analysis software (Volume Graphics 3.04 software).

The SSM samples were embedded in a bakelite thermosetting resin with carbon filler suitable for Scanning electron microscope (SEM) examination. Sample preparation was carried out on a Struers Tegramin automatic polisher, with a final grinding step equivalent to 1200 grit paper and subsequent polishing with 1 and 0.25 μm diamond suspension. A brief etching step using Keller's etchant (approximately 10 s) was applied to unveil the processed zone and particles' distribution. Additionally, a 2 nm carbon layer was sputtered to cover non-conductive particles. Optical micrographs, illustrating macroscopic features of the processed zones, guided the selection of locations for energy dispersive x-ray spectroscopy (EDX) measurements. Scanning electron microscope (SEM) and EDX analyses were conducted using a Zeiss Merlin VP compact SEM with a Bruker XFlash EDX detector. The accelerating voltage was 15 kV, and the working distances were approximately between [12, 22] mm.

X-ray diffraction (XRD) characterization was conducted using a PANalytical X'Pert Pro MDP diffractometer equipped with a cobalt anode (Co Kα radiation) and a 1D X'Celerator detector. Measurements were conducted by continuous scanning in the 20–90°(2θ) range, and XRD data were analysed using High Score Plus software. These analyses were performed on a sample extracted from the nugget region to determine the presence of PZT and BT particles in the SSM samples and to assess whether the thermomechanical processing induced by FPS could cause any structural changes in these particles.

For Vickers microhardness profiling, a Mitutoyo HM-112 hardness testing machine applied a 1.0 kgf load for 10 s along the Y direction of the processed plate. Electrical conductivity measurements were performed using eddy currents and potential drop techniques along a straight line in the Y direction (refer to figure 1). The top 1 mm of the sample surface was machined, and a pencil probe operating at 1 MHz and a NORTEC 600D impedance analyser was used for eddy currents. Potential drop measurement utilized a standard Jandel^{TM} linear four-point probe with a Keithley SourceMeter 2450 and a Keithley Nanovoltmeter 2182 A.

Uniaxial tensile test specimens were created using a HAAS Super Mini Mill 2 CNC Machining Centre, following the standards of ASTM E8/E8M-13a. These test specimens were used to assess the mechanical properties of the SSM. The testing was conducted at room temperature, using a servo-hydraulic MTS 312.21 testing machine with a load capacity of 100 kN. Fracture surface analysis was performed by SEM using a Hitachi High-Tech SU3800.

Sensorial properties of the SSM were assessed by measuring the electrical response to cyclic loads using a universal testing equipment MTS 312.21, a Keithley Nanovoltmeter 2182 A, and a National Instruments DAQ assisted by a LabView program. The electrical response behaviour and sensorial properties of the SSM based on PZT and BT particles were characterized through cyclic load tests and by measuring the electrical response at five different frequencies (0.063, 0.125, 0.250, 0.500 Hz, and 1.000 Hz), according to the procedure previously described by Ferreira *et al* [45]. It should be noted that the intensity of the cyclic loads applied is below the yield strength of the SSM [45], meaning it remains within the elastic domain.

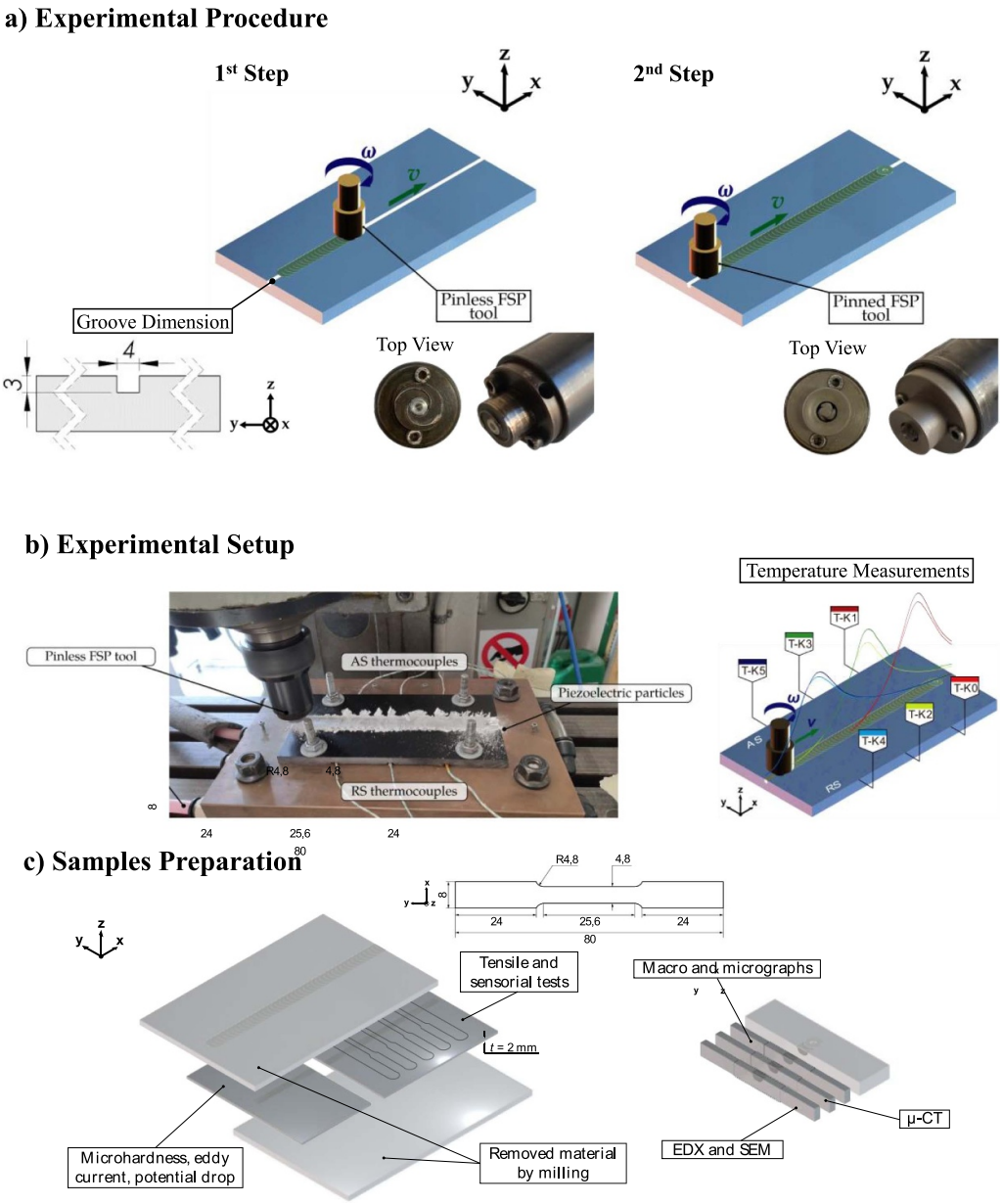

Figure 1. Features of the SSM fabrication process.

3. Results and discussion

3.1. Characterisation of manufacturing process

Initially, it was imperative to establish the optimal processing parameters for AA2017-T451 alloys and ensuring an optimal distribution of particles. According to the present authors previous study [45], ensuring a uniform and concentrated distribution of particles in the nugget leads to enhanced sensitivity in the SSM. In this context, a series of tests was established to ensure that the process parameters used would result in a uniform particle distribution in the stir zone. This involved varying the travel speed (ν) at rates of 71, 90, and 112 mm min^{-1}, with a constant rotation speed (ω) maintained at 1120 rev min^{-1}. The cross-sectional macrographs depicting the processed regions of the AA2017 alloys are detailed in figure 2.

Upon meticulous examination of the cross-sections of the processed regions, distinctive linear defects were observed in the lower section of the nugget, specifically on the AS. Notably, these defects did not originate from the processing itself but rather resulted from a misalignment between the tool pin and the groove machined in the plate.

Based on the analysis of the surface quality of the processed area, the particle distribution within the nugget, and the identification of defects during the processing, it has been determined that the ideal parameters for achieving an effective particle distribution are $\nu = 71$ mm min^{-1} and $\omega = 1120$ rev min^{-1} for the AA2017 alloy.

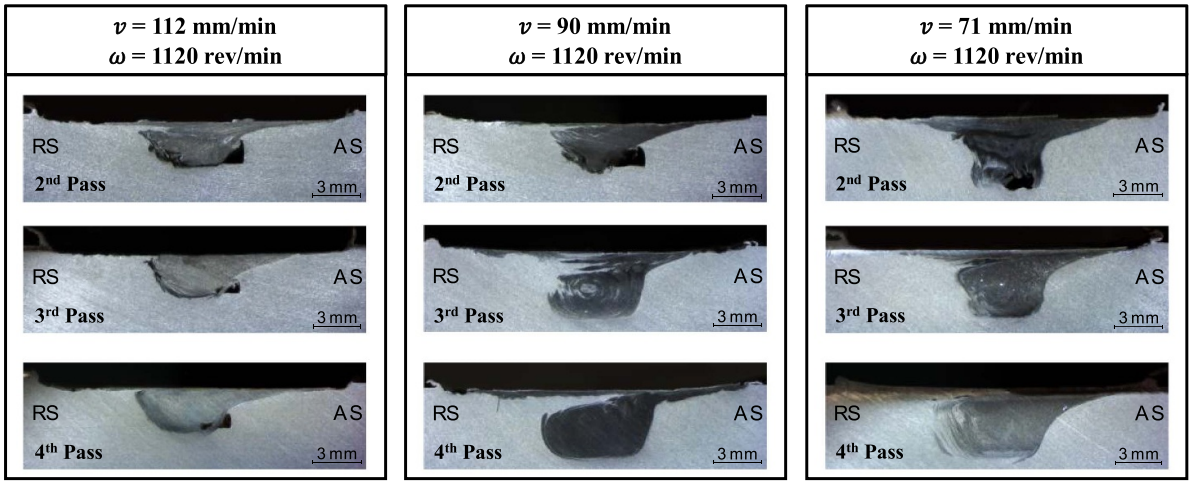

Figure 2. Processing parameters improvement for AA2017-T451.

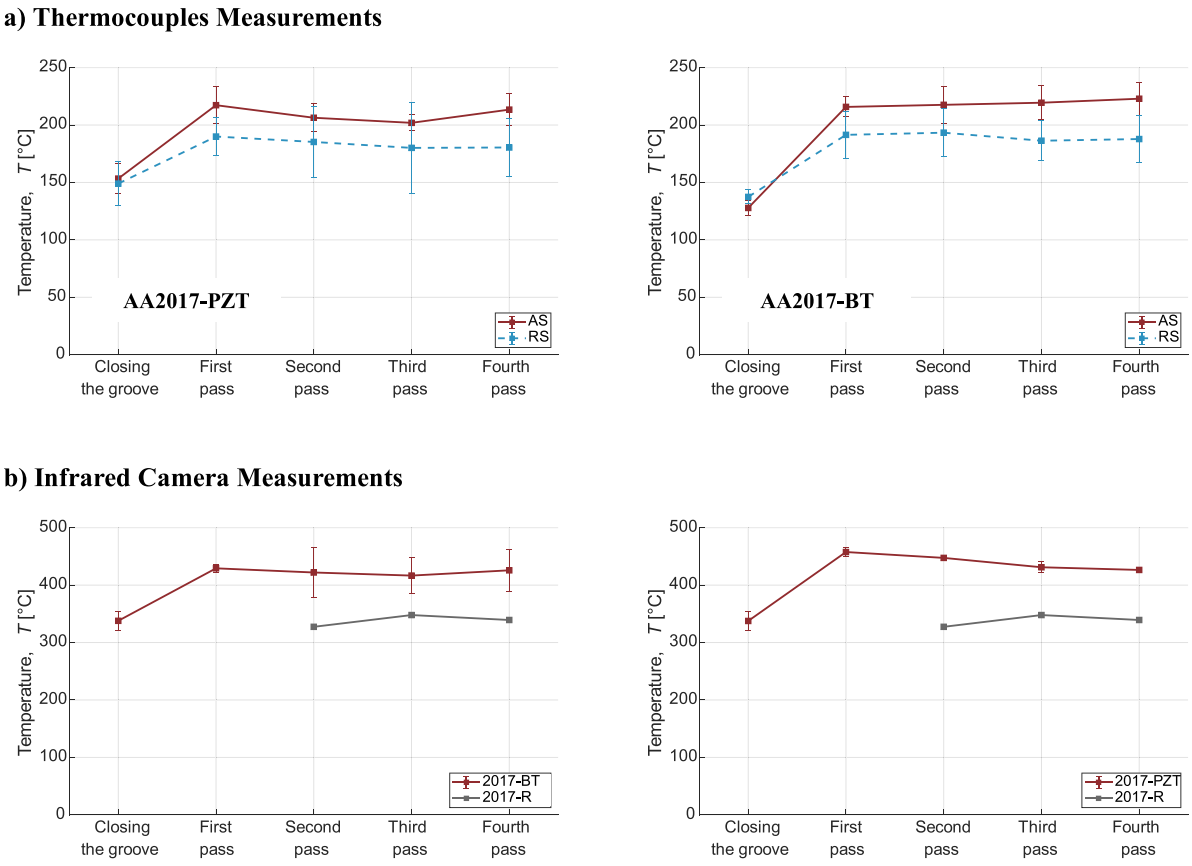

Figure 3. Maximum temperatures were recorded by the thermocouples and infrared camera at the surface of the stir zone for each pass.

Figure 3(a) illustrates the maximum temperatures recorded by the thermocouples at the AS and RS during each pass of the SSM processing. In addition, the utilization of different piezoelectric particles for embedding did not result in significant variations in the maximum temperature. It is important to note that the presented data primarily represents the temperature evolution throughout plate processing and may not precisely depict the temperature reached in the nugget region. To address this, the thermal imaging camera recorded the maximum temperature at the surface of the stir zone during each pass, as depicted in figure 3(b).

During the groove closing stage, temperatures were lower and remained nearly constant during the processing stage, as evident in figure 3. The plastic deformation occurring during the groove closing process, facilitated by the pinless FSP tool, is confined to the plate surface, leading to lower heat generation compared to subsequent processing passes. In the processing stage with the pinned FSP tool, plastic deformation

intensifies, resulting in increased heat generation. Figure 3(b) indicates that, during the processing stage, the maximum temperatures at each pass remain relatively constant, hovering around 450 °C for AA2017-PZT plates and 430 °C for AA2017-BT plates. Consequently, the peak temperature remains consistent regardless of the number of passes when employing identical processing parameters and tools. The data from both thermocouples and the thermal imaging camera reveal significantly lower temperatures during the groove closing phase compared to subsequent processing passes. This discrepancy is attributed to the reduced plastic deformation induced by the pinless FSP tool, resulting in lower temperature generation. Importantly, the number of passes does not appear to influence the processing temperature, as the maximum temperature remains relatively constant during the four processing passes.

A comparison of maximum temperatures recorded by thermocouples and the thermal imaging camera for plate processing situations, with and without particles, indicates an anticipated increase in temperatures when particles are incorporated. The introduction of ceramic particles into the aluminium matrix adds complexity, requiring additional energy for effective dispersion and embedding. Moreover, the presence of ceramic particles in the nugget tends to decrease the composite's thermal conductivity (Al-based alloys + particles), which reduces the thermal flow and leads to high local temperatures and a greater thermal gradient, such as observed for arc-based welding joint of alloys with low and high thermal conductivity, respectively [53].

3.2. Characterisation of SSMs

3.2.1. Metallographic and physicochemical characterization. The examination of particle dispersion within the processed region, commonly referred to as the nugget, and the identification of key microstructural regions, such as the heat-affected zone (HAZ) and the thermo-mechanically affected zone (TMAZ), was achieved through the utilization of both macro and microstructural characterization techniques. In figures 4(a) and 5(a), the macro and micrographs of the AA2017-BT and AA2017-PZT samples are presented, respectively.

FSP has effectively promoted the distribution of particles in both aluminium matrix alloys. A prior EDX analysis conducted by Ferreira *et al* [43] for AA5083-H111 demonstrated that darker regions within the stir zone correlate with higher concentrations of piezoelectric particles. Consequently, the processing of AA2017 generally resulted in a distribution of piezoelectric particles in the region influenced by the pin. Moreover, macrographs indicate that particles exhibit a more homogeneous distribution in the AS compared to the RS.

Macrographs, particularly those emphasizing the region influenced by the shoulder, as exemplified by the AA2017-BT in figure 4(a), reveal a less uniform particle distribution within this area, characterized by larger agglomerates and occasional processing defects. It is essential to note, however, that specimens utilized in uniaxial and sensorial behaviour tests possess a thickness (t) of 2 mm, measured from the bottom part of the nugget, thereby excluding this less homogeneous region.

Figure 4(b) depicts the EDX maps at low magnification of the zone influenced by the pin and the shoulder in the AA2017-BT sample. A heterogeneous distribution can be observed in the region influenced by the shoulder, with substantial particles' agglomerates, whereas the region influenced by the pin is much more homogeneous and has smaller agglomerates. EDX maps at higher magnification inside the region influenced by the pin reveal the distribution of particles within this region having some small agglomerates, as depicted in figure 4(c). SEM images revealed the structure and morphology of these small agglomerates and point spectrum analysis confirms the presence of BT particles confined in the aluminium matrix (figure 4(d)).

The EDX map of the AA2017-PZT sample at low magnification, presented in figure 5(b), revealed larger agglomerates than the AA2017-BT sample. Nevertheless, the particles' overall distribution inside the stir zone's central region remains very homogeneous.

SEM images at higher magnification were taken to characterize the structure and morphology of this agglomerate and its surrounding particles, depicted in figure 5(d), and point spectrum analyses were conducted to identify its constituent elements. The chemical composition (wt%) of all the analysed particles corresponds to PZT particles confined inside the aluminium matrix, except particle 5, which appears to be a fragment of the pinned FSP tool, given the high iron content.

Figure 6(a) provides a visual representation of the essential microstructural aspects of aluminium processing in the absence of particles. Within this context, the HAZ exhibits larger grains than the base material, a consequence of the heat generated throughout the processing phase. In contrast, the TMAZ showcases the combined influence of heat and substantial strain, manifested by elongated and deformed grains.

The stir zone, on the other hand, manifests clear indications of dynamic recrystallization. This phenomenon arises from the intense plastic deformation that the material undergoes at elevated temperatures, leading to a refinement of the grain structure. These distinct microstructural regions collectively illustrate the intricate interplay of heat, strain, and plastic deformation in the aluminium processing cycle.

Figure 6(b) presents the EDX maps of the main constituents of the AA2017-R sample inside the central region of the stir zone. The small, lighter particles observed in the SEM image appear to be related to precipitates of mainly copper, while the darker particles seem to be related to magnesium-based precipitates.

Upon comparing the grain size within the stir zone before and after the introduction of piezoelectric particles, it becomes apparent that the incorporation of these particles led to a more intense grain size refinement in the AA2017 alloy. Prior research has emphasized the significant role played by reinforcement particles in the fragmentation of grains within the processed microstructure, attributed to localized

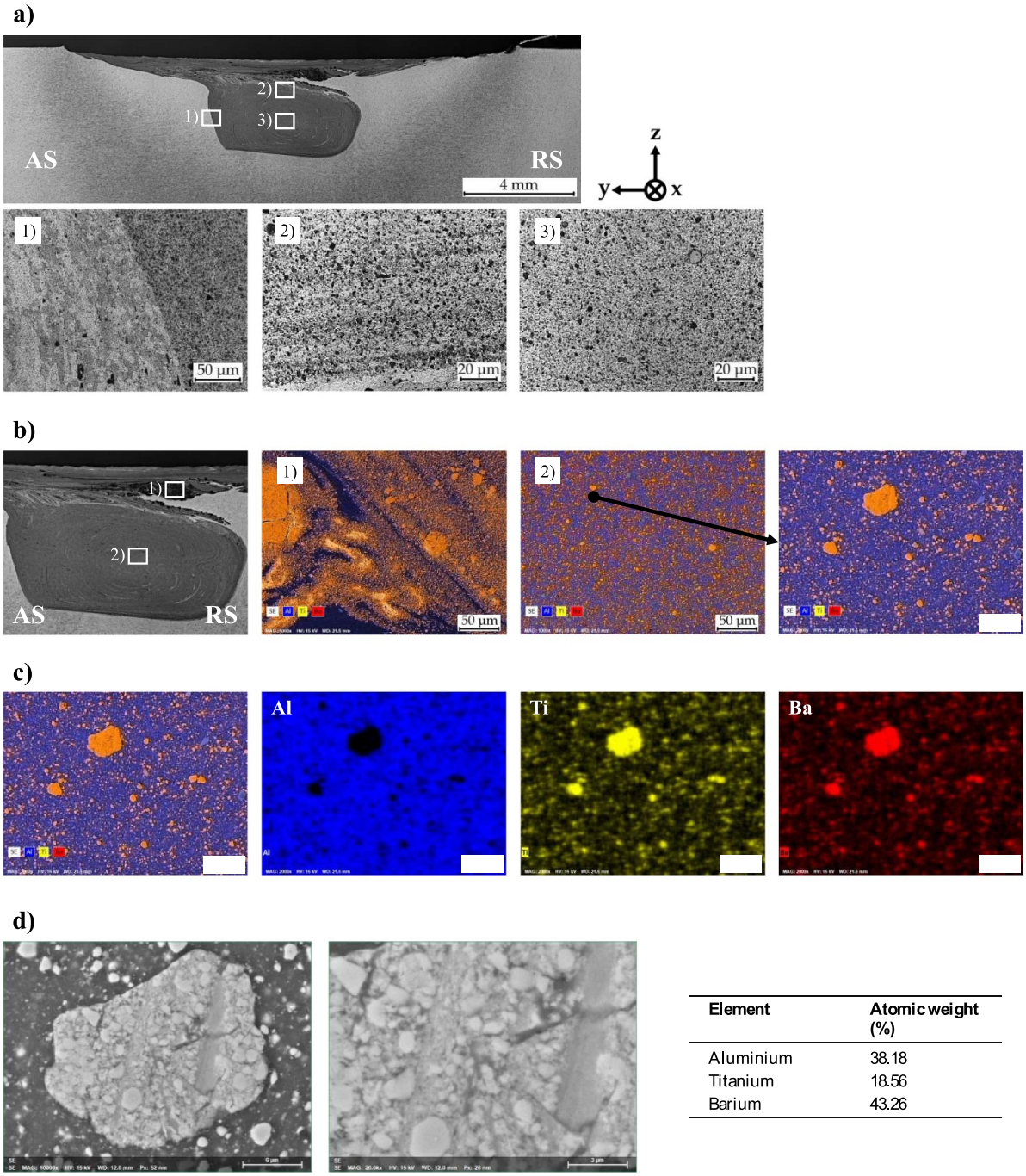

Element	Atomic weight (%)
Aluminium	38.18
Titanium	18.56
Barium	43.26

Figure 4. Macrostructural and physicochemical characterization of particles' distribution of AA2017-BT: (a) macro and microstructural characterisation; (b) optical macrograph of stir zone and EDX maps of the zone influenced by the shoulder (b1) and the zone influenced by the pin (b2) at x1000 magnification; (c) EDX maps of the zone influenced by the pin, at x2000 magnification; (d) SEM image and point spectrum analysis of the largest particle agglomerate found in the central zone of the nugget.

and non-uniform deformation [54]. Additionally, the utilization of reinforcement particles acts as a constraint on the grain growth of the aluminium matrix grains, known as the Zener pinning effect [55].

Microscopic examinations of the stir zone in the SSMs processed with PZT revealed a greater prevalence of larger particle agglomerates in comparison to those embedded with BT. This observation can be predominantly ascribed to the morphology of the PZT particles, which are often an order of magnitude larger than BT particles and exhibit a proclivity to form agglomerates more readily. This distinction can significantly influence grain refinement in the microstructure, as smaller particles tend to exert a more pronounced effect on grain refinement than their larger counterparts [55].

The distribution of particles was assessed through μCT analysis, as illustrated in figures 7 and 8. An inclusive analysis was additionally carried out to examine the presence of internal agglomerates within the processed zone. The results

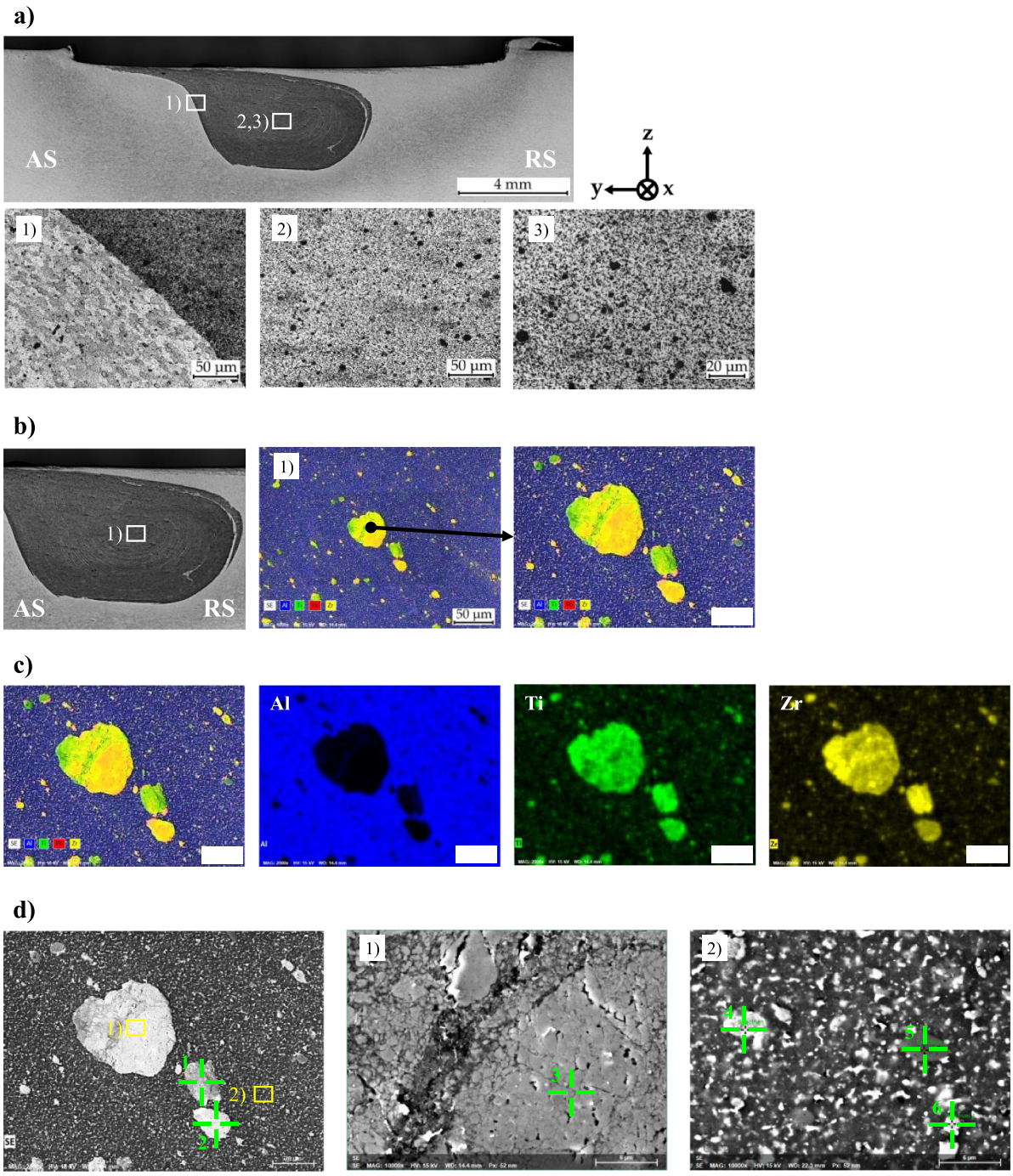

Spectrum	Lead	Zirconium	Titanium	Oxygen	Aluminium	Magnesium	Copper	Manganese	Iron
Particle 1	53.51	23.72	11.11	6.63	4.51	0.52	-	-	-
Particle 2	72.41	11.70	10.44	3.93	1.52	-	-	-	-
Particle 3	80.05	9.03	7.25	2.22	1.44	-	-	-	-
Particle 4	64.14	17.96	8.29	6.08	3.54	-	-	-	-
Particle 5	-	-	-	-	61.96	-	6.48	17.44	14.12
Particle 6	67.99	18.97	7.68	-	5.36	-	-	-	-

Figure 5. Macrostructural and physicochemical characterization of particles' distribution of AA2017-PZT: (a) macro and microstructural characterisation; (b) optical macrograph of stir zone and EDX map of the zone influenced by the pin, at x1000 magnification; (c) EDX maps of the zone influenced by the pin, at x2000 magnification; (d) SEM images and point spectrum analysis (wt%) of the larger particle agglomerate found in the central zone of the nugget and the surrounding particles.

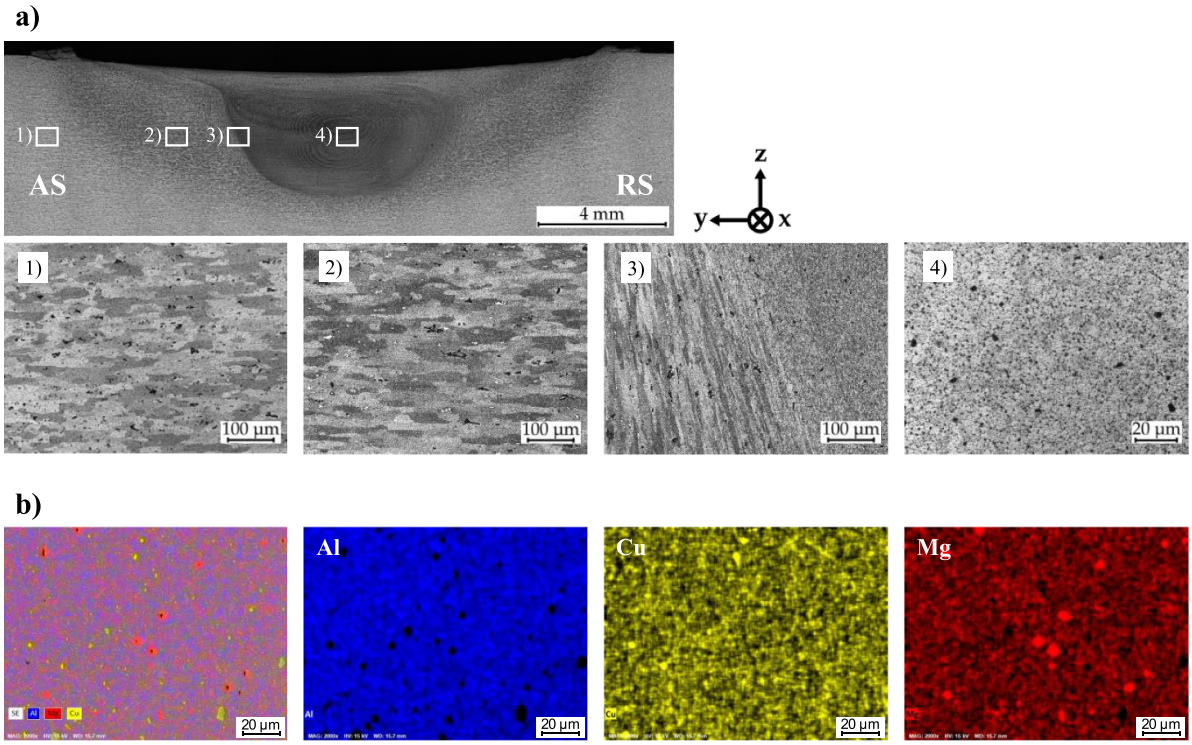

Figure 6. Macrostructural and physicochemical characterization of AA2017-R: (a) macro and microstructural characterisation; (b) SEM image and EDX maps of the centre zone influenced by the pin, at x1000 magnification.

for AA2017, involving both BT and PZT particles, are presented in figures 7 and 8, respectively. These results unveiled a relatively uniform spatial distribution of particles along the Y and Z directions. However, within the region influenced by the shoulder, particles tended to form agglomerates, resulting in a less homogeneous distribution compared to the central region of the nugget. In the AA2017-BT sample, larger volume agglomerates were observed in the shoulder-influenced region, in contrast to the AA2017-PZT sample, where this region was less extensive and only exhibited minor particle agglomerates.

To establish a comprehensive understanding of the relationship between the inclusion analysis and the presence of agglomerates, a comparative analysis, depicted in figures 7 and 8, was conducted between the μCT data and the macrographs of the SSMs.

The μCT images reveal higher concentrations of piezoelectric particles on the RS of the nugget and at the interface between the regions influenced by the shoulder and the pin for both AA2017-BT and AA2017-PZT samples. In these regions, the inclusion analysis exposed localized agglomerates of particles, distinguishable by a bright white coloration shown in figures 7(j) and 8(j). Macrographs of these samples corroborate the presence of particle agglomerates in these regions, as indicated by a darker coloration.

XRD analysis conducted on the processed region of AA2017-BT, AA2017-PZT, and AA2017-R specimens highlights the presence of BT and PZT particles in the stirred zone, as depicted in figure 9. The AA2017-BT sample (figure 9(a) distinctly exhibits BT particles, with reflections at 24.95° corresponding to the (100) and (001) reflections of the tetragonal structure. The more prominent peaks around 36.01° represent the (101) and (011) reflections of this structure [43]. The XRD pattern for AA2017-PZT (figure 9(b)) also confirms the presence of PZT particles, primarily evidenced by the main reflection at 35.96°.

Figure 9 reveals reflections associated with the Al phase and Cu-containing intermetallic compounds. This latter can be associated with the precipitate evolution during the multiple FSP thermal cycles, which can induce the transition from Guinier–Preston zone (naturally aged) to Al_2Cu (θ, overaged condition). In addition, the BT and PZT particles tend to increase the peak temperature and reduce the cooling rate (section 3.1), which also corroborated the presence of the Al_2Cu (θ) phase in the nugget region [56].

Furthermore, the XRD analysis identifies the presence of Mg and Si-rich compounds. The consistent observation of Mg_2Si precipitates, regardless of the applied degree of deformation, is noteworthy. These precipitates have been previously observed in aluminium alloys with even lower concentrations of Mg and Si [57].

3.2.2. Mechanical and electrical characterization. The mechanical performance of the SSMs was evaluated through uniaxial tensile tests, with figures 10(a), (e) and (i) representing the engineering stress/strain curves, while figures 10(b)–(d), (f)–(h), and (j)–(l) depict the fractured samples and their respective fracture surfaces.

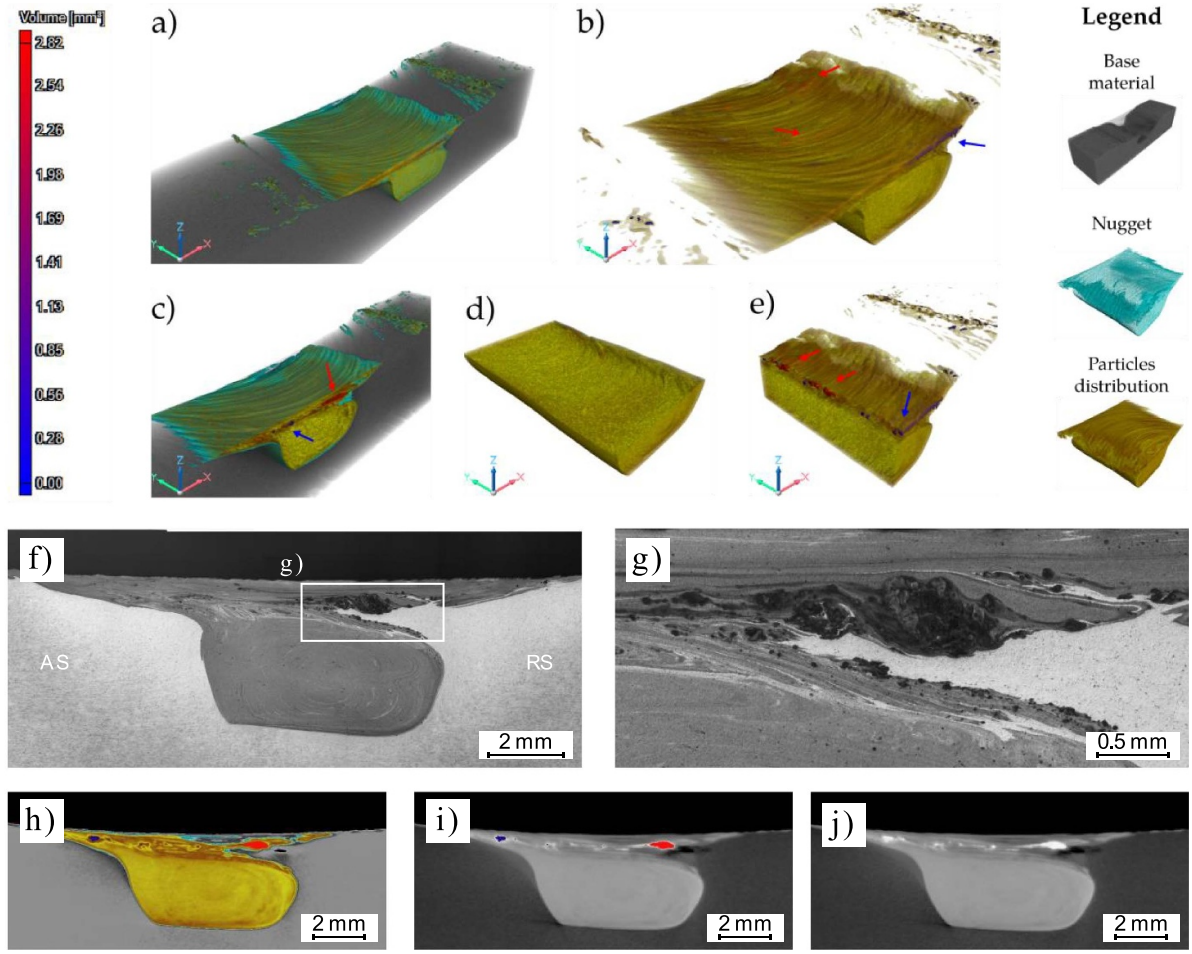

Figure 7. Comprehensive understanding of the inclusion analyses and its relation with the particles' distribution: μCT analysis of AA2017-BT (sample (a), particles' distribution (b), transversal cross section of the sample (c), longitudinal cross section of the nugget ((d), (e)); comparison between the macrographs ((f), (g)) and μ-CT images ((h)–(j)) of SSM.

A comparison between the processing of plates with and without the incorporation of particles suggests that the yield strength ($\sigma_{0.2}$) does not exhibit significant changes when particles are introduced, as evidenced in table 4. Nevertheless, the inclusion of PZT particles renders the SSM more susceptible to brittleness compared to the addition of BT particles, as the elongation at fracture significantly decreases. Figures 10(g) and (h) illustrates the fractured specimens containing PZT particles. In contrast to figures 10(c) and (d), which pertains to the incorporation of BT particles, the fractures in the PZT specimens precisely occur within the zone containing the particles, i.e. the stir zone. This occurrence may suggest a weak bond between the PZT particles and the aluminium matrix, possibly attributed to the irregular and larger-sized morphology of the particles. The PZT particles exhibit a feeble connection with the Al matrix, offering no reinforcing effect and, in certain cases, potentially concentrating stresses, thereby reducing the yield limit. Regarding the σ_{UTS}, it diminishes compared to AA2017-R due to the increased brittleness of the material resulting from the fragile nature of ceramic particles that rapidly fracture or detach from the matrix under load. This impedes the effective transfer of stress to the matrix. While uniform deformation occurs across the material within the elastic region, entering the plastic region of aluminium (reaching the yield point) results in non-uniform deformation between the particles and the matrix, leading to matrix fracture and subsequent rapid fracture propagation (low ductility). As AA2017-PZT lacks ductility with no hardening occurring, the σ_{UTS} tends to closely approach the yield strength.

Examining the fracture surfaces of the SSM processed with AA2017 in figures 10(b)–(d), (f)–(h), (j)–(l), the failure mode is clearly ductile, with well-defined dimples present on all fracture surfaces. The fracture has occurred along a 45° plane, indicating a consistent pattern. In the case of AA2017-BT, the fracture has extended outside the processed zone, like the sample processed without particles (as shown in figures 10(i)–(l). As a result, both fracture surfaces shared similarities. While AA2017-PZT fractured at the interface between the processed zone and the base material, it suggests that the fracture happened through the PZT particles themselves.

Particle distribution, microhardness measurements, eddy current testing, and potential drop measurements were conducted on both processed and non-processed regions of the plate's transverse section (*Y* direction). Figure 11 displays the results obtained for AA2017 alloys.

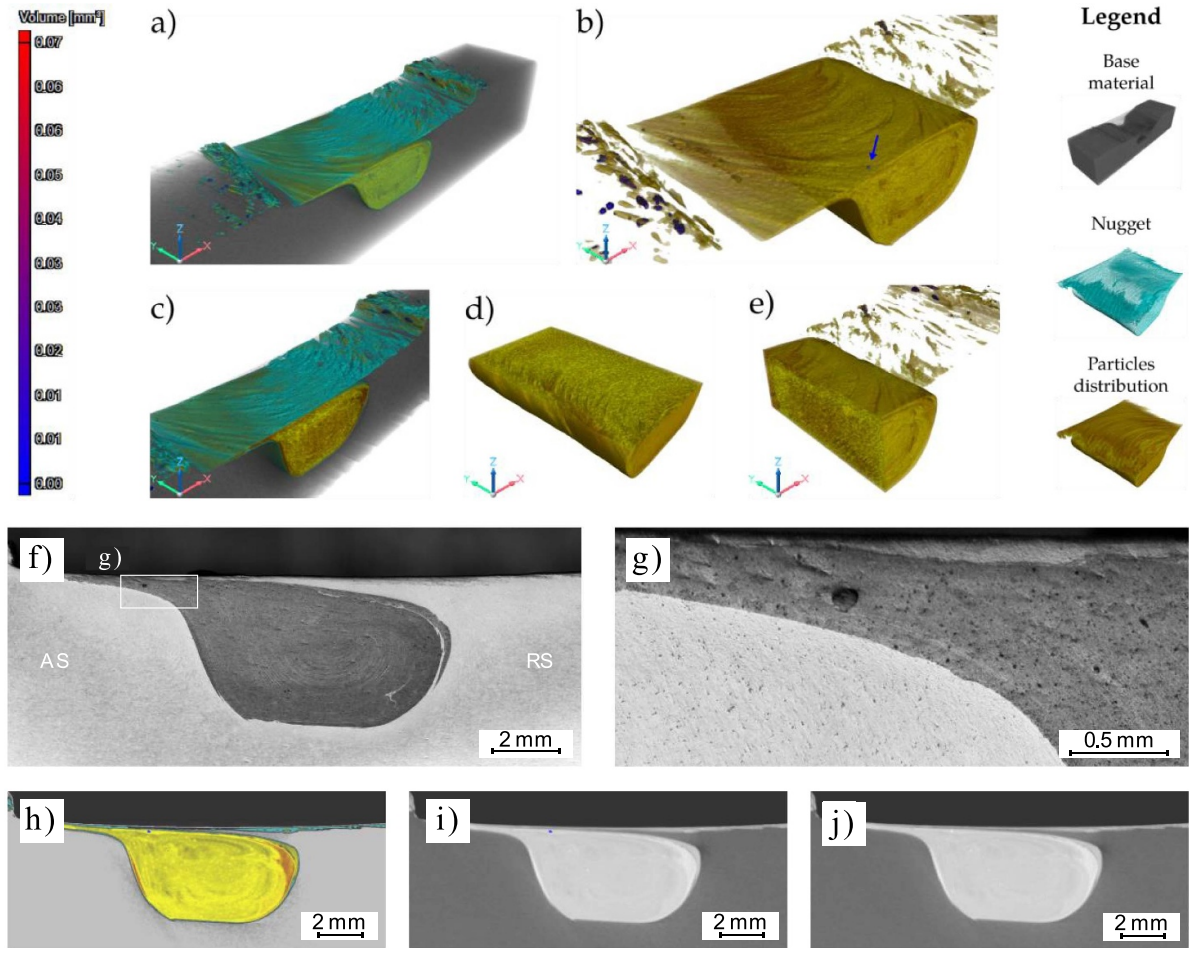

Figure 8. Comprehensive understanding of the inclusion analyses and its relation with the particles' distribution: μCT analysis of AA2017-PZT (sample (a), particles' distribution (b), transversal cross section of the sample (c), longitudinal cross section of the nugget ((d), (e)); comparison between the macrographs ((f), (g)) and μ-CT images ((h)–(j)) of SSM.

Hardness measurements serve as an indicator of changes in mechanical strength, as they are directly proportional to it. Potential drop measurements enable the acquisition of resistivity and conductivity values in both processed and non-processed zones. Previous studies [58, 59] have demonstrated that electrical conductivity is inversely proportional to hardness, and consequently, strength. Eddy's current testing, a technique used to assess microstructural changes in materials, complements hardness measurements. As a result, processed zones exhibit lower electrical conductivity due to increased grain boundaries, which reduce electronic mobility and enhance hardness. Conversely, thermally affected zones demonstrate higher conductivity and reduced hardness, attributed to grain growth [58, 59].

Based on the obtained results, it can be observed that the hardness in unaffected zones, i.e., in the base material, remains relatively constant, with average values of 120 HV1.0 and electrical conductivity close to 30 IACS (%). These values are consistent with the expected theoretical values of 118 HV and 34 IACS (%). As explained previously, maximum electrical conductivity values are recorded in the HAZ and, consequently, minimum hardness values due to grain coalescence. Therefore, the low temperature annealing experienced during processing reduces the strengthening effect caused by the T451 heat treatment. However, a clear distinction in hardness within the stir zone is evident between the BT and PZT particles processing. The samples processed with BT particles exhibit an increase in hardness of approximately 20–30 HV1.0, whereas the samples processed with PZT particles even show a hardness decrease of up to 10 HV1.0 in the stir zone. These results are consistent with the micrographs presented in section 3.2.1. It can be observed that the BT particles present in the micrographs corresponding to the nugget zone have a significantly smaller size compared to the samples processed with PZT particles. Furthermore, as previously mentioned, smaller particles have a more pronounced impact on grain refinement, which may explain why the hardness increases when processing is conducted with BT particles and tends to decrease with PZT particles.

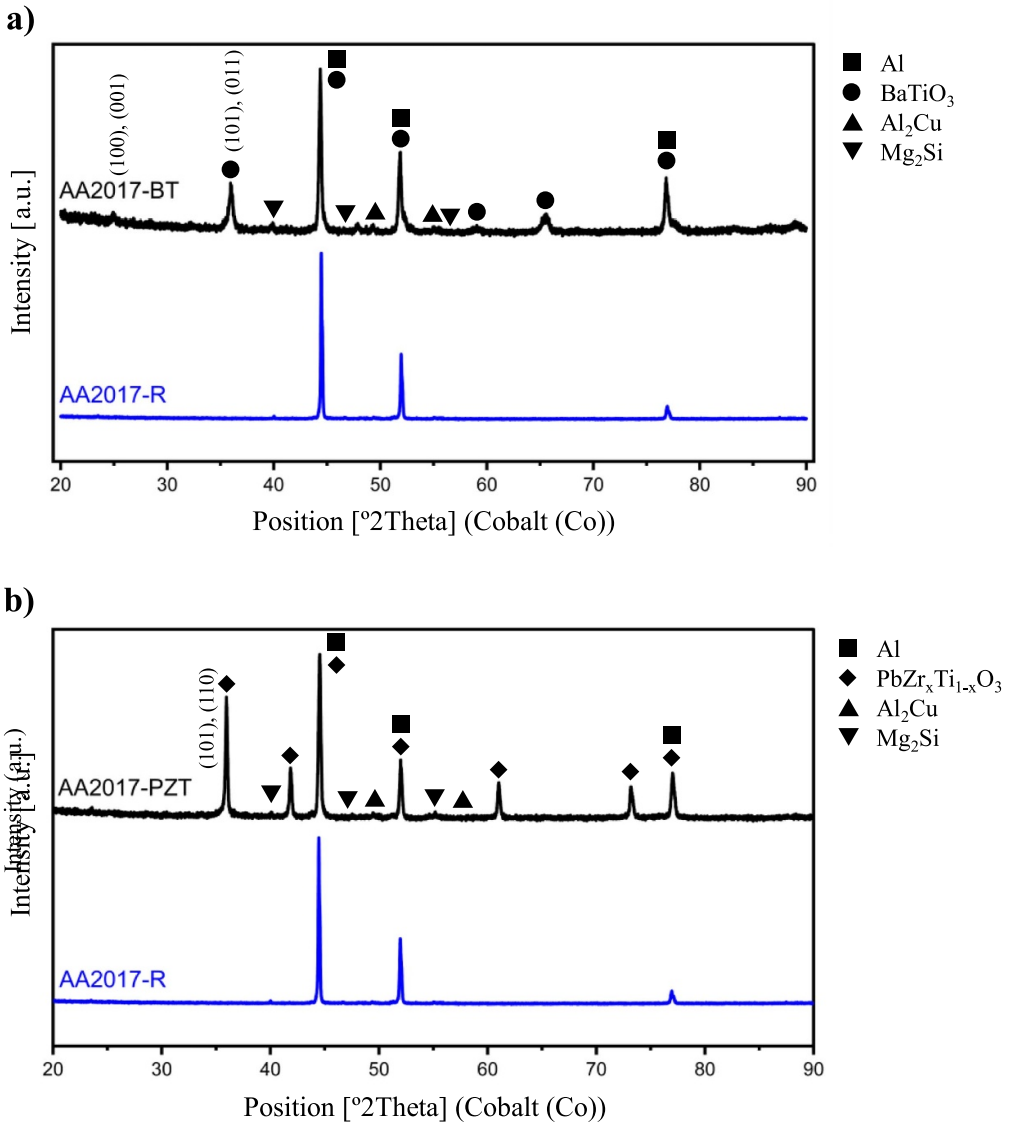

Figure 9. X-ray diffractogram for the SSM studied: (a) AA2017-BT; (b) AA2017-PZT.

3.2.3. Sensorial properties assessment. The sensorial properties were assessed by submitting the SSM samples to a set of cyclic loads while measuring their electrical response. Figure 12 depicts the process involved in calculating the sensitivity of the SSM samples.

These experiments were replicated for all SSM-produced samples and conducted under varying frequencies. Figure 13 depicts the response of AA2017 with distinct embedded piezoelectric particles, namely BT and PZT. The results demonstrate the anticipated linear correlation between applied load and electrical response, consistent with findings by Ferreira *et al* [43, 45]. Higher sensitivities were observed at lower frequencies overall, except for AA2017-BT, where the sensitivity at 0.125 Hz surpassed that at 0.063 Hz.

Figure 14 illustrates the effect on sensitivity when incorporating PZT and BT particles into the AA2017 matrix. The outcomes reveal a trend toward achieving higher sensitivities with the inclusion of PZT particles compared to BT particles, despite the seemingly anomalous sensitivity of AA2017-BT at $f = 0.125$ Hz. This difference may be attributed to the higher piezoelectric constant of PZT particles ($d_{33}/d_{31} = 270/-120$ pC N^{-1}) compared to BT particles ($d_{33}/d_{31} = 190/-78$ pC N^{-1}). Furthermore, the maximum sensitivity of the AA2017-PZT sample, 21.71×10^{-4} μV MPa^{-1}, exceeded that of AA2017-BT by 43%, registering 15.16×10^{-4} μV MPa^{-1}.

To assess the response under impulse loading, a series of single punctual loads with an amplitude (A) of 0.100 mm and different frequencies (f) were applied to the SSMs, as illustrated in figure 15. As expected, the SSMs remained responsive under the impulse loads, exhibiting a response with the same frequency as the loading and confirming their capability to detect loading at various frequencies.

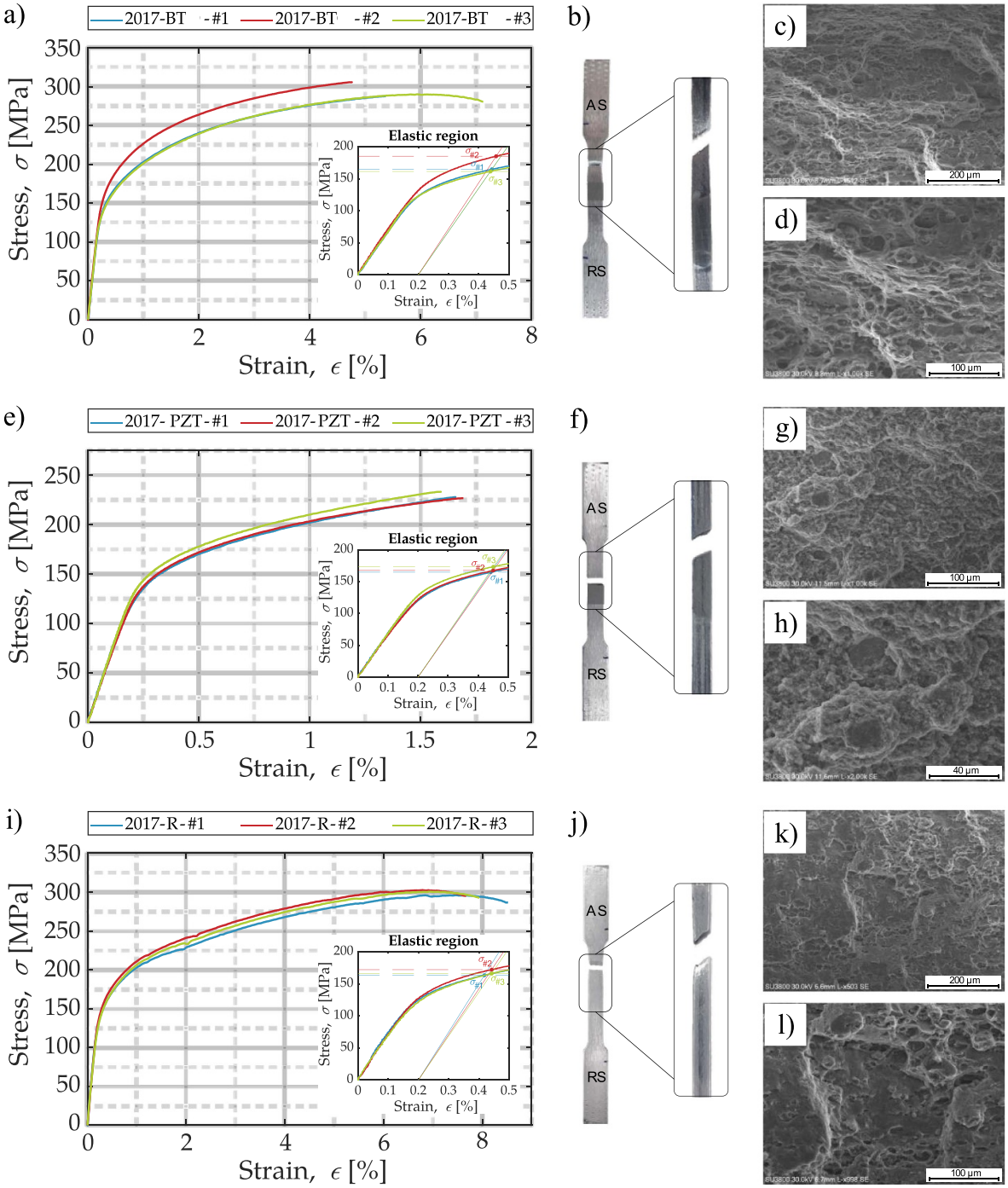

Figure 10. Uniaxial tensile tests of AA2017-BT (a)–(c), AA2017-PZT (e)–(h) and AA2017-R (i)–(l): engineering stress-strain curves ((a), (e), (i)); fractured #3 sample ((b), (f), (j)); fractured surface of SSM ((c), (d), (g), (h), (k), (l)).

Piezoelectric particles are incorporated into a metallic matrix made of aluminium, which provides a conductive environment. Despite the conductive nature of the matrix, it is still possible to obtain an electrical voltage response proportional to the applied load, regardless of the type of piezoelectric particles used (whether PZT or BT), as demonstrated in figures 13 and 14. Furthermore, figure 11 reveals that the electrical conductivity in the regions where the particles are embedded decreases from 30 IACS (%) to 25 IACS (%) for AA2017-BT, and to 26 IACS (%) for AA2017-PZT. This reduction is expected due to decreased electron mobility caused by the presence of ceramic particles and a refined grain structure. The decrease in conductivity, and the resulting reduced electron mobility, can enhance the piezoelectric effect in the composite, facilitating an electrical response when subjected to loading.

Figure 16 illustrates a comparison of sensitivity results obtained by incorporating PZT particles into metallic matrices,

Table 4. Mechanical properties withdrawn from uniaxial tests.

Sample reference	Yield strength, $\sigma_{0.2}$ (MPa)	Modulus of elasticity, E (GPa)	Ultimate tensile strength, σ_{UTS} (MPa)	Strain at fracture, ε_f
AA2017-BT-#1	164.64	67.55	287.77	5.37
AA2017-BT-#2	185.23	71.78	305.85	4.76
AA2017-BT-#3	161.36	67.55	290.28	7.12
AA2017-PZT-#1	164.72	68.03	227.89	1.66
AA2017-PZT-#2	167.49	66.80	226.74	1.69
AA2017-PZT-#3	173.03	69.01	233.22	1.59
AA2017-R-#1	163.25	74.84	295.96	8.52
AA2017-R-#2	172.04	70.99	302.50	7.67
AA2017-R-#3	165.89	68.48	300.49	7.93

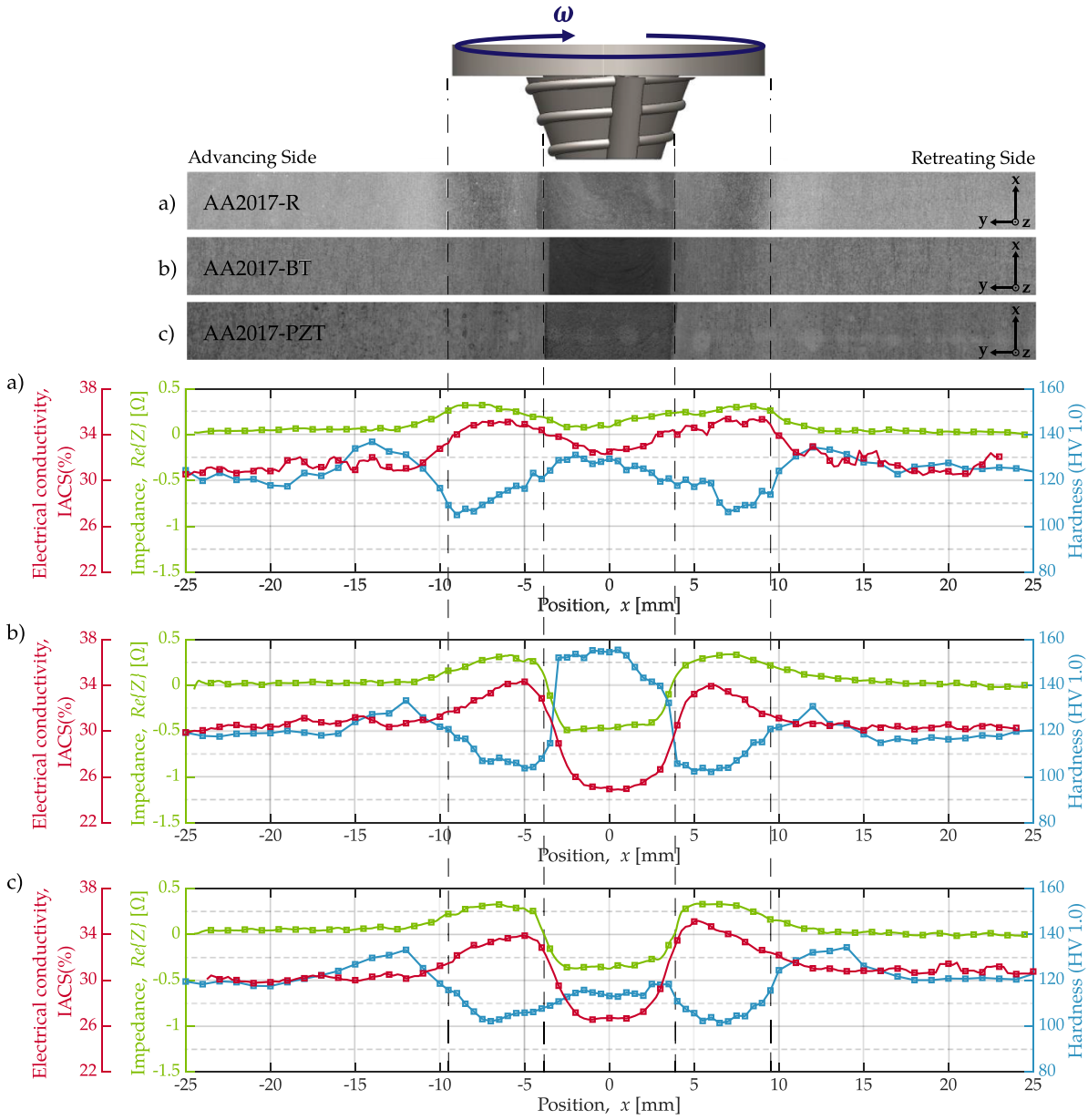

Figure 11. Profiles of microhardness, electrical conductivity, and impedance of AA2017 samples.

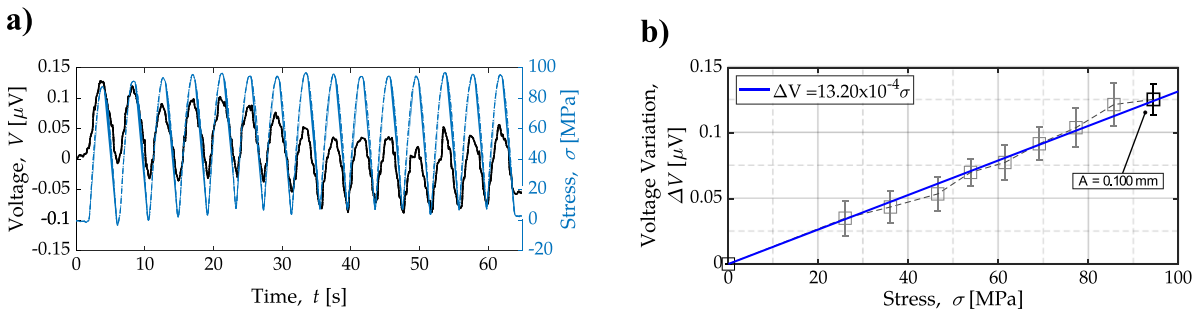

Figure 12. The process involved in calculating the sensibility of AA2017-PZT: (a) cyclic loading at $f = 0.125$ Hz and $A = 0.100$ mm, set of 15 cycles; (b) sensitivity at $f = 0.125$ Hz, with all set of amplitudes.

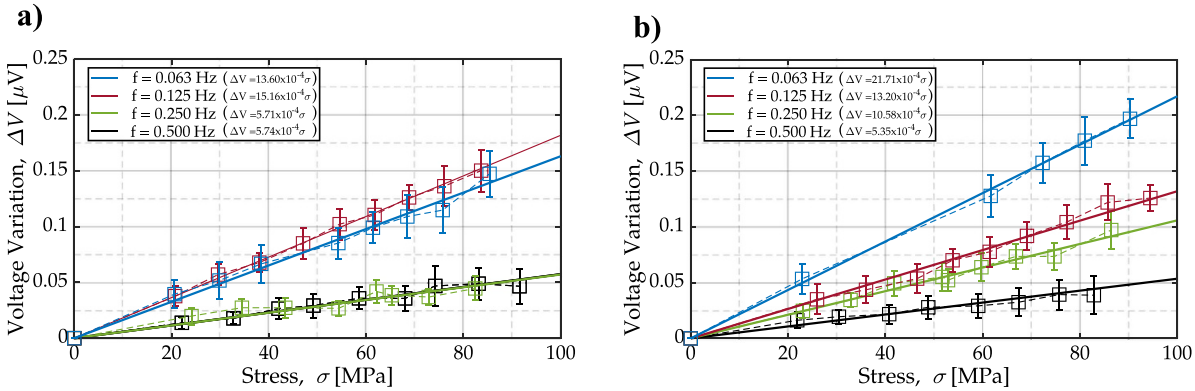

Figure 13. Electrical response to cycle loads and the effect of different load frequencies on the electric response of the SSM: (a) AA2017-BT; (b) AA2017-PZT.

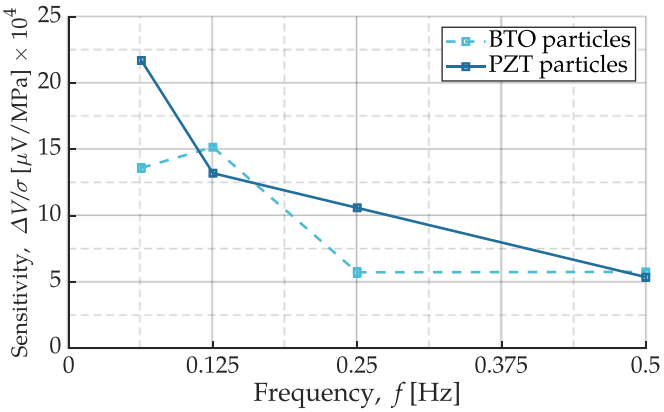

Figure 14. Sensitivity of the effect of embedding different piezoelectric particles in the AA2017-T451 matrix.

specifically the AA2017-T451 and AA5083-H111 alloys. The sensitivity of AA2017-PZT samples exhibited superior performance compared to AA2017-BT samples, as previously confirmed. To further contextualize these findings, the results of AA2017-PZT samples were juxtaposed with Ferreira *et al* research data refer to the AA5083-H111 alloy [43]. PZT particles embedded in an AA5083-H111 matrix exhibited higher sensitivity than the inclusion of BT particles. Based on the interpretation of figure 16, it can be inferred that embedding PZT particles in AA2017-T451 alloy results in sensitivity 30%–60% lower than that of AA5083-H111 across all tested frequencies. Furthermore, an increase in frequency accentuates the disparity in sensitivity between these alloys. When PZT particles are incorporated into these aluminium alloys, a SSM with higher sensitivity is obtained when compared to the usage of BT particles. However, the use of PZT particles causes more agglomerates, making the SSM more fragile and with inferior mechanical behaviour. Despite these challenges, using FSP as a particle inclusion technique to create materials with sensory properties is a viable option.

Based on current literature, it is believed that incorporating piezoelectric ceramic powder into a metal matrix can lead to

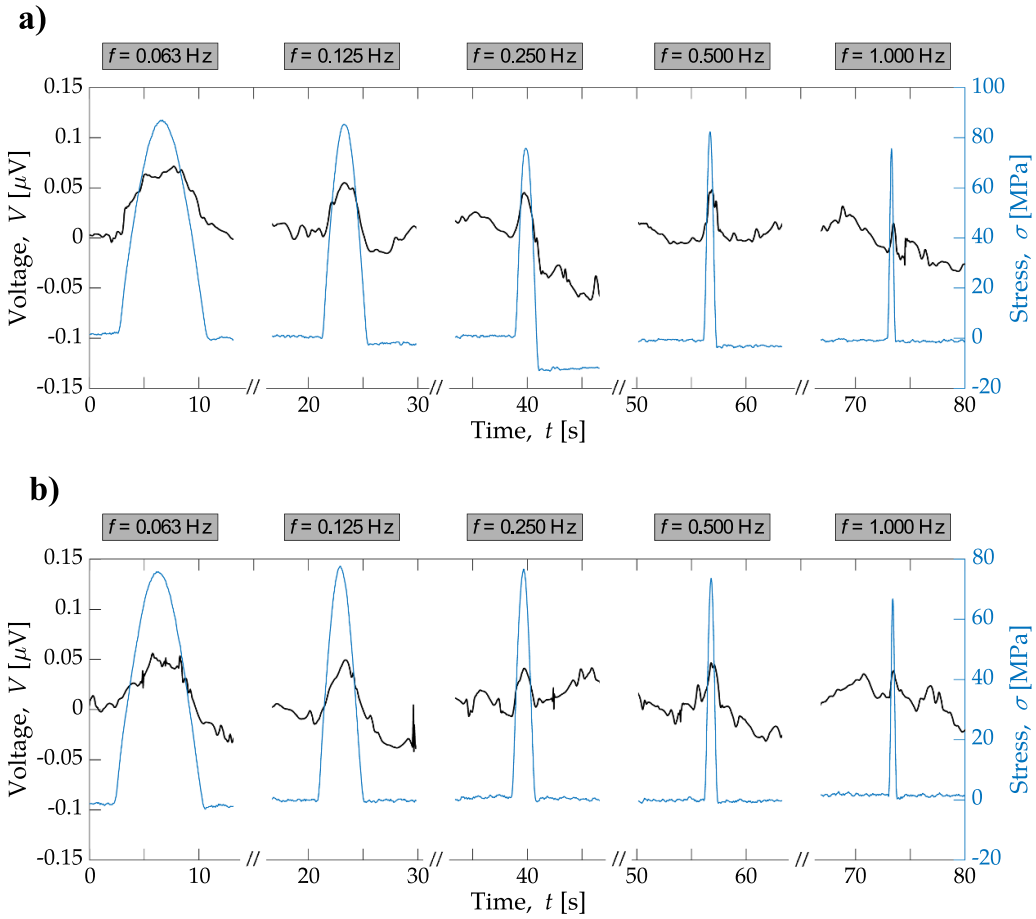

Figure 15. Electrical response of SSMs to impulse loading with different frequencies: (a) AA2017-BT; (b) AA2017-PZT.

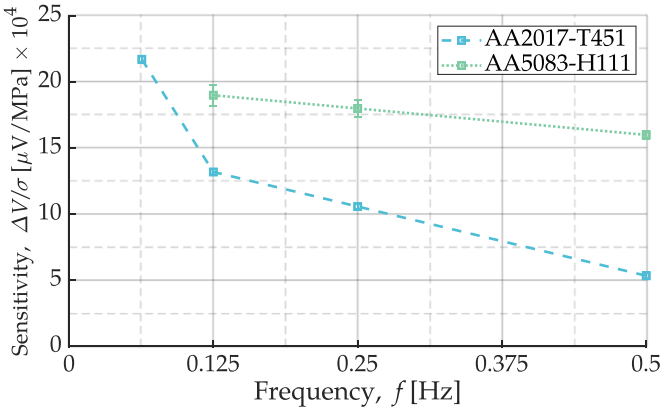

Figure 16. Comparison of sensitivity results obtained by incorporating PZT particles into metallic matrices, specifically the AA2017-T451 and AA5083-H111 alloys.

an activated piezoelectric effect through mechanical deformation of the PZT and BT particles. The creation of composites with metal matrices and piezoelectric particles as reinforcement, like Bismuth ferrite/BT [60] or Copper/BT [61], has demonstrated that it is possible to produce functional materials with the potential to exhibit the piezoelectric effect.

4. Conclusion

This study has successfully demonstrated the feasibility of imparting sensorial properties to heat-treated AA2017-T451 by incorporating BT and PZT particles, resulting in a SSM capable of responding to external loading. Under cyclic loading, the SSMs exhibit a linear correspondence between applied load and electrical response at the same frequency. Sensorial characterization unveiled an inverse and non-linear relationship between frequency and sensitivity, indicating the SSMs' suitability for low-frequency applications. Furthermore, PZT particle embedment generally provided better sensitivities than BT particles, with their electrical response exhibiting proportionality with loads. In addition, temperature measurements indicate that the addition of piezoelectric particles increases process complexity, leading to higher processing temperatures compared to particle-free processing. Thermal camera measurements revealed a 22%–30% increase in maximum processing temperatures with the introduction of piezoelectric particles.

Metallographic and physicochemical characterizations provided a deeper understanding of particle distribution. The embedding of BT and PZT particles in AA2017 resulted in a homogeneous particle distribution in the region influenced

by the pin. Uniaxial tests results revealed increased material brittleness with the incorporation of piezoelectric particles, particularly with PZT. While the failure mode of AA2017 SSMs without particles was ductile fracture, the embedment of PZT resulted in brittle fracture, with the fracture surface perpendicular to the loading. The bonding between PZT particles and the aluminium matrix appeared weaker than with BT particles, as evidenced by fracture occurring precisely in the stir zone. Yield strength did not change significantly with particle embedment, but the FSP resulted in a lower ultimate strength compared to pre-processing levels. The impact of low temperature annealing during FSP was confirmed by a decrease in the hardness of the TMAZ compared to the base material. Hardness measurements indicated increased hardness in the stir zone with BT embedment, contrasting with a slight decrease with PZT embedment. Micrographs and fracture analysis aligned with these findings, revealed larger agglomerates and fractures within the stir zone for PZT, suggesting weaker bonding between particles and the metal matrix. Eddy's current testing and potential drop measurements were consistent with registered hardness profiles. So, incorporating PZT particles into aluminium alloys results in a SSM that exhibits greater sensitivity compared to utilizing BT particles. Nevertheless, the inclusion of PZT particles leads to increased agglomeration, rendering the SSM more fragile with inferior mechanical behaviour. Despite these challenges, employing FSP as a technique for particle inclusion to generate materials with sensory properties remains a viable option.

The sensitivity of SSM based on PZT and BT particles tends to decrease as load frequency increases. In the context of civil engineering, structures generally have a low fundamental mode frequency, which makes this SSM very useful. However, in mechanical and aerospace industries, the modes of interest are typically in the high-frequency range, where the sensitivity of SSM based on PZT and BT particles is notably reduced. Therefore, future work should focus on refining and implementing this SSM technology within metal components used in civil engineering, as well as developing methods to enhance SSM sensitivity in high-frequency applications. This would broaden the scope of SSM's usability in these sectors.

Data availability statement

All data that support the findings of this study are included within the article (and any supplementary files).

Acknowledgments

PMF acknowledges FCT—Fundação para a Ciência e a Tecnologia for funding the PhD Grant UI/BD/151055/2021. PM F, M A M, C V and M S C acknowledge FCT—Fundação para a Ciência e a Tecnologia for its financial support via Projects UIDB/00667/2020 and UIDP/00667/2020 (UNIDEMI). F W C F acknowledges Fundação para a Ciência e a Tecnologia (FCT-MCTES) for funding the PhD Grant 2022.13870.BD.

Author statement

Pedro M Ferreira: Conceptualization, Methodology, Formal analysis, Investigation, Data curation, Writing-Original draft preparation, Visualization. **David Caçador:** Conceptualization, Methodology, Formal analysis, Writing- Reviewing and Editing. **Miguel A Machado:** Conceptualization, Methodology, Formal analysis, Writing- Reviewing and Editing. **Marta S Carvalho:** Conceptualization, Methodology, Formal analysis, Writing-Reviewing and Editing. **Pedro Vilaça:** Formal analysis, Writing- Reviewing and Editing. **Gonçalo Sorger:** Formal analysis, Writing- Reviewing and Editing. **Francisco Werley Cipriano Farias:** Formal analysis, Writing- Reviewing and Editing. **Arthur Ribeiro Figueiredo:** Formal analysis, Writing- Reviewing and Editing. **Catarina Vidal:** Conceptualization, Methodology, Formal analysis, Resources, Writing- Reviewing and Editing, Supervision, Project administration, Funding acquisition.

Conflict of interest

The authors declare that there is no conflict of interest.

ORCID iDs

Pedro M Ferreira https://orcid.org/0000-0002-5344-898X
Miguel A Machado https://orcid.org/0000-0001-9352-5196

References

[1] Anton S R and Sodano H A 2007 A review of power harvesting using piezoelectric materials (2003–2006) *Smart Mater. Struct.* **16** R1–21
[2] Ferreira P M, Machado M A, Carvalho M S and Vidal C 2022 Embedded sensors for structural health monitoring: methodologies and applications review *Sensors* **22** 8320
[3] Mirjalili A, Aval H J and Serajzadeh S 2013 An investigation into the microstructure of friction-stir welded and artificially aged AA2017 *J. Mater. Eng. Perform.* **22** 3566–71
[4] Yanaseko T, Asanuma H and Sato H 2015 Characterization of a metal-core piezoelectric ceramics fiber/aluminum composite *Mech. Eng. J.* **2** 14–00357
[5] Najjari A, Mehdinavaz Aghdam R, Ebrahimi S A S, Suresh S K, Krishnan S, Shanthi C and Ramalingam M 2022 Smart piezoelectric biomaterials for tissue engineering and regenerative medicine: a review *Biomed. Tech.* **67** 71–88
[6] Esther L, Piselli A, Faucheu J, Delafosse D and Del Curto B 2014 Smart materials: development of new sensory experiences through stimuli responsive materials *5th STS Italia Conf. A Matter of Design: Making Society through Science and Technology* (*Milan, Italy*)
[7] Bogue R 2014 Smart materials: a review of capabilities and applications *Assem. Autom.* **34** 16–22
[8] McCABE J F, Yan Z, Al Naimi O T, Mahmoud G and Rolland S L 2009 Smart materials in dentistry-future prospects *Dent. Mater. J.* **28** 37–43
[9] Li H, Tian C and Deng Z D 2014 Energy harvesting from low frequency applications using piezoelectric materials *Appl. Phys. Rev.* **1** 041301

[10] Mahapatra S D, Mohapatra P C, Aria A I, Christie G, Mishra Y K, Hofmann S and Thakur V K 2021 Piezoelectric materials for energy harvesting and sensing applications: roadmap for future smart materials *Adv. Sci.* **8** 2100864

[11] Uchino K 2017 The development of piezoelectric materials and the new perspective *Advanced Piezoelectric Materials* (Elsevier) pp 1–92

[12] Korkmaz S and Kariper I A 2022 $BaTiO_3$-based nanogenerators: fundamentals and current status *J. Electroceram.* **48** 8–34

[13] Gallego-Juarez J A 1989 Piezoelectric ceramics and ultrasonic transducers *J. Phys. E: Sci. Instrum.* E **22** 804–16

[14] Jiao P, Egbe K-J I, Xie Y, Matin Nazar A and Alavi A H 2020 Piezoelectric sensing techniques in structural health monitoring: a state-of-the-art review *Sensors* **20** 3730

[15] Chen Y and Xue X 2018 Advances in the structural health monitoring of bridges using piezoelectric transducers *Sensors* **18** 4312

[16] Sekhar M C, Veena E, Kumar N S, Naidu K C B, Mallikarjuna A and Basha D B 2023 A review on piezoelectric materials and their applications *Cryst. Res. Technol.* **58** 2200130

[17] Basheer A A 2020 Advances in the smart materials applications in the aerospace industries *Aircr. Eng. Aerosp. Technol.* **92** 1027–35

[18] Gao X, Yang J, Wu J, Xin X, Li Z, Yuan X, Shen X and Dong S 2020 Piezoelectric actuators and motors: materials, designs, and applications *Adv. Mater. Technol.* **5** 1900716

[19] Kuruveri U B, Panemangalore D B, Kuruveri S B, John M and Menezes P L 2022 Surface modification of 6xxx series aluminum alloys *Coatings* **12** 180

[20] Soujon M, Kallien Z, Roos A, Zeller-Plumhoff B and Klusemann B 2022 Fundamental study of multi-track friction surfacing deposits for dissimilar aluminum alloys with application to additive manufacturing *Mater. Des.* **219** 110786

[21] Hasan M S, Kordijazi A, Rohatgi P K and Nosonovsky M 2022 Application of triboinformatics approach in tribological studies of aluminum alloys and aluminum-graphite metal matrix composites *Minerals, Metals & Materials Series* (Springer) pp 41–51

[22] Sandeep R and Natarajan A 2022 Application of machine learning approaches to predict joint strength of friction stir welded aluminium alloy 7475 and PPS polymer hybrid joint *Proc. Inst. Mech. Eng.* C **236** 9003–11

[23] Chen J, Cui B, Daniels J E, Wang J, Gu Q, Jiang Y, Cheng Z, Cheng J and Zhang S 2023 Understanding the strain mechanisms in $BiFeO_3$-$BaTiO_3$ piezoelectric ceramics near the morphotropic phase boundary *J. Eur. Ceram. Soc.* **43** 4766–73

[24] Bian L *et al* 2022 Performance enhancement of ultrasonic transducer made of textured PNN-PZT ceramic *J. Adv. Dielectr.* **12** 2244003

[25] Smith M and Kar-Narayan S 2022 Piezoelectric polymers: theory, challenges and opportunities *Int. Mater. Rev.* **67** 65–88

[26] Mohammadpourfazeli S, Arash S, Ansari A, Yang S, Mallick K and Bagherzadeh R 2023 Future prospects and recent developments of polyvinylidene fluoride (PVDF) piezoelectric polymer; fabrication methods, structure, and electro-mechanical properties *RSC Adv.* **13** 370–87

[27] Su Y *et al* 2022 High-performance piezoelectric composites via β phase programming *Nat. Commun.* **13** 4867

[28] Wang Z, Maruyama K and Narita F 2022 A novel manufacturing method and structural design of functionally graded piezoelectric composites for energy-harvesting *Mater. Des.* **214** 110371

[29] Wang R, Sui J and Wang X 2022 Natural piezoelectric biomaterials: a biocompatible and sustainable building block for biomedical devices *ACS Nano* **16** 17708–28

[30] Devi H S and Maisnam M 2022 Lead-free piezoelectric nanostructures and their applications *Materials Horizons: From Nature to Nanomaterials* (Springer) pp 343–57

[31] Bhadwal N, Ben Mrad R and Behdinan K 2023 Review of zinc oxide piezoelectric nanogenerators: piezoelectric properties, composite structures and power output *Sensors* **23** 3859

[32] Mishra S R, Fard S H, Sheikh T and Behdinan K 2022 Electromechanical performance of biocompatible piezoelectric thin-films *Actuators* **11** 171

[33] Shu Y J, Shen F, Ke L L and Wang Y S 2022 Adaptive finite element simulation and experimental verification for fretting wear of PVDF piezoelectric thin films *Wear* **502–503** 204395

[34] Wei J, He C, Qie M, Li Y, Tian N, Qin G and Zuo L 2023 Achieving high performance of wire arc additive manufactured Mg–Y–Nd alloy assisted by interlayer friction stir processing *J. Mater. Process. Technol.* **311** 117809

[35] Eivani A R, Mehdizade M, Ghosh M and Jafarian H R 2023 The effect of multi-pass friction stir processing on microstructure, mechanical properties, and corrosion behavior of WE43-nHA bio-composite *J. Mater. Res. Technol.* **22** 776–94

[36] Dwivedi S P, Kumar I, Sehgal S, Gupta N and Saxena K K 2023 Development of dissimilar AA2014 and AA2024 based composite with nano-Si_3N_4 reinforcement by friction stir process technique *J. Adhes. Sci. Technol.* **38** 687–703

[37] Dwivedi S P, Sharma S, Li C, Zhang Y, Kumar A, Singh R, Eldin S M and Abbas M 2023 Effect of nano-TiO_2 particles addition on dissimilar AA2024 and AA2014 based composite developed by friction stir process technique *J. Mater. Res. Technol.* **26** 1872–81

[38] Singla S, Sagar P and Handa A 2023 Recent advances in magnesium-based metal matrix surface composites developed via friction stir processing route—an overview *Metallogr. Microstruct. Anal.* **12** 385–400

[39] Węglowski M S 2018 Friction stir processing—state of the art *Arch. Civ. Mech. Eng.* **18** 114–29

[40] Ma Z Y 2008 Friction stir processing technology: a review *Metall. Mater. Trans.* A **39** 642–58

[41] Vidal C, Ferreira P M, Ferreira F B, Buinho M, Silva T T and Santos T G 2023 Improving the stability of the friction stir channelling technology via a cooled copper backing plate *Int. J. Adv. Manuf. Technol.* **129** 525–46

[42] Vaira Vignesh R, Padmanaban R and Datta M 2018 Influence of FSP on the microstructure, microhardness, intergranular corrosion susceptibility and wear resistance of AA5083 alloy *Tribol.—Mater. Surf. Interfaces* **12** 157–69

[43] Ferreira P M, Machado M A, Carvalho M S, Vilaça P, Sorger G, Pinto J V, Deuermeier J and Vidal C 2023 Self-sensing metallic material based on PZT particles produced by friction stir processing envisaging structural health monitoring applications *Mater. Charact.* **205** 113371

[44] Ferreira P M, Machado M A, Carvalho M S and Vidal C 2023 Self-sensing metallic material based on piezoelectric particles *Res. Rev. J. Nondestruct. Test.* **1** 1

[45] Ferreira P M, Machado M A, Carvalho M S and Vidal C 2023 Granting sensorial properties to metal parts through friction stir processing *Measurement* **207** 112405

[46] Vidal C, Ferreira P M, Inácio P L, Ferreira F B, Santiago D, Meneses P, Silva R J C and Santos T G 2023 Particles' distribution enhancing in aluminum-based composites produced by upward friction stir processing *Int. J. Adv. Manuf. Technol.* **127** 2745–57

[47] Moreira F, Ferreira P M, Silva R J C, Santos T G and Vidal C 2023 Aluminium-based dissimilar alloys surface composites reinforced with functional microparticles produced by upward friction stir processing *Coatings* **13** 962
[48] Yang J 2018 *An Introduction to the Theory of Piezoelectricity* vol 9 (Springer International Publishing)
[49] Freire Filho F C M, Santos J A, Sanches A O, Medeiros E S, Malmonge J A and Silva M J 2023 Dielectric, electric, and piezoelectric properties of three-phase piezoelectric composite based on castor-oil polyurethane, lead zirconate titanate particles and multiwall carbon nanotubes *J. Appl. Polym. Sci.* **140** e53572
[50] Mohamad S, Liza S and Yaakob Y 2020 Strengthening of the mechanical and tribological properties of composite oxide film formed on aluminum alloy with the addition of graphite *Surf. Coat. Technol.* **403** 126435
[51] Olasumboye A, Owolabi G, Odeshi A, Zeytinci A and Yilmaz N 2018 Dynamic response and microstructure evolution of AA2219-T4 and AA2219-T6 aluminum alloys *J. Dyn. Behav. Mater.* **4** 162–78
[52] Vidal C, Alves P, Alves M M, Carmezim M J, Fernandes M H, Grenho L, Inácio P L, Ferreira F B, Santos T G and Santos C 2022 Fabrication of a biodegradable and cytocompatible magnesium/nanohydroxyapatite/fluorapatite composite by upward friction stir processing for biomedical applications *J. Mech. Behav. Biomed. Mater.* **129** 105137
[53] Aghaee Attar M, Ghoreishi M and Malekshahi Beiranvand Z 2020 Prediction of weld geometry, temperature contour and strain distribution in disk laser welding of dissimilar joining between copper & 304 stainless steel *Optik* **219** 165288
[54] Parumandla N and Adepu K 2018 Effect of Al2O3 and SiC nano reinforcements on microstructure, mechanical and wear properties of surface nanocomposites fabricated by friction stir processing *Medziagotyra* **24** 338–44
[55] Su J Q, Nelson T W, Mishra R and Mahoney M 2003 Microstructural investigation of friction stir welded 7050-T651 aluminium *Acta Mater.* **51** 713–29
[56] Chen Y C, Feng J C and Liu H J 2009 Precipitate evolution in friction stir welding of 2219-T6 aluminum alloys *Mater. Charact.* **60** 476–81
[57] Cabibbo M and Evangelista E 2006 A TEM study of the combined effect of severe plastic deformation and (Zr), (Sc+Zr)-containing dispersoids on an Al–Mg–Si alloy *J. Mater. Sci.* **41** 5329–38
[58] Santos T G, Miranda R M, Vilaça P, Teixeira J P and Dos Santos J 2011 Microstructural mapping of friction stir welded AA 7075-T6 and AlMgSc alloys using electrical conductivity *Sci. Technol. Weld. Join.* **16** 630–5
[59] Sorger G L, Oliveira J P, Inácio P L, Enzinger N, Vilaça P, Miranda R M and Santos T G 2019 Non-destructive microstructural analysis by electrical conductivity: comparison with hardness measurements in different materials *J. Mater. Sci. Technol.* **35** 360–8
[60] Zheng T and Wu J 2022 Origin of large piezoelectricity in BF-BT based multiphase ferroelectrics *Ceram. Int.* **48** 23808–13
[61] Lemkova V, Todt J, Motz C and Schaefer F 2023 Metal–matrix composites from high-pressure torsion with functionalized material behavior *Adv. Eng. Mater.* **25** 2201565